Perpendicular-anisotropy artificial spin ice with spontaneous ordering: a platform for reservoir computing with flexible timescales

Check for updates

Aleksandr Kurenkov [1,2] ✉, Jonathan Maes [3] ✉, Aleksandra Pac[1,2], Gavin Martin Macauley [1,2], Bartel Van Waeyenberge[3], Aleš Hrabec [1,2] ✉ & Laura Jane Heyderman [1,2]

Arrays of coupled nanomagnets have wide-ranging fundamental and practical applications in artificial spin ices, reservoir computing and spintronics. However, lacking in these fields are nanomagnets with perpendicular magnetic anisotropy with sufficient magnetostatic interaction. This would not only open up unexplored possibilities for artificial spin ice geometries but also enable novel coupling methods for applications. Here, we demonstrate a method to engineer the energy landscape of artificial spin lattices with perpendicular magnetic anisotropy. With this, we are able to realize for the first time strongly magnetostatically-coupled 2D lattices of out-of-plane Ising spins that spontaneously order at room temperature on timescales that can be precisely engineered. We show how this property, together with straightforward electrical interfacing, make this system a promising platform for reservoir computing. Our results open the way to investigate the thermodynamics of out-of-plane magnetostatically coupled nanomagnet arrays with novel spin ice geometries, as well as to exploit such nanomagnet arrays in unconventional computing, taking advantage of the adjustable temporal dynamics and strong coupling between nanomagnets.

Coupled nanomagnets organized on the sites of various lattices are widely-explored in the field of artificial spin ice[1–3] since they exhibit a large variety of fascinating phenomena including collective dynamics[4–6], frustration[7–9], dynamic chirality[10] and phase transitions[11–13]. Furthermore, these properties can be exploited for novel forms of conventional[14–19] and unconventional[20–24] computing. The single-domain nanomagnets typically have an in-plane magnetic anisotropy, which results in strong magnetostatic coupling between the magnets due to extended demagnetizing fields in the lattice plane. In contrast, dipolar-coupled nanomagnets with perpendicular magnetic anisotropy have rarely been employed for artificial spin ice because they have not shown spontaneous ordering–so they are not "thermally-active"–at experimentally measurable timescales[25–30]. This lack of spontaneous evolution makes such magnets a common choice for high-density bit-patterned media[31,32].

Creating lattices comprised of magnetostatically coupled nanomagnets with perpendicular anisotropy that show spontaneous ordering on an experimentally-accessible timescale would open the way to study

the thermodynamics of out-of-plane artificial spin ices based on a large variety of lattices. Among them are the lattices associated with the crystal planes of many bulk magnetic systems[33–35], the triangular lattice[36,37], and the canonical two-dimensional (2D) Ising model on the square lattice[38–40]. While any of these lattices can be created with the method described in this work, we will focus on the latter due to its broad importance and universality. Being universally complete, so that any other statistical model[41,42] or Boolean circuit[43,44] can be derived from it, the 2D Ising model is of fundamental importance for statistical physics and has been used to model numerous physical, mathematical and biological processes[45–47]. The modelling is typically carried out by selecting a particular variant of the model, setting an initial state, and then observing how it evolves into a lower-energy state over time. The nature of this evolution provides a means to solve non-deterministic polynomial-time (NP-) hard problems with only polynomial overhead (P-hard) by mapping them onto a corresponding Ising system[48,49]. Since any NP-hard problem can be formulated as an Ising problem, the 2D Ising system is of

[1]Laboratory for Mesoscopic Systems, Department of Materials, ETH Zurich, Zurich, Switzerland. [2]PSI Center for Neutron and Muon Sciences, Villigen PSI, Switzerland. [3]DyNaMat, Department of Solid State Sciences, Ghent University, Ghent, Belgium. ✉e-mail: kurenkovalexander@gmail.com; jonathan.maes@ugent.be; ales.hrabec@psi.ch
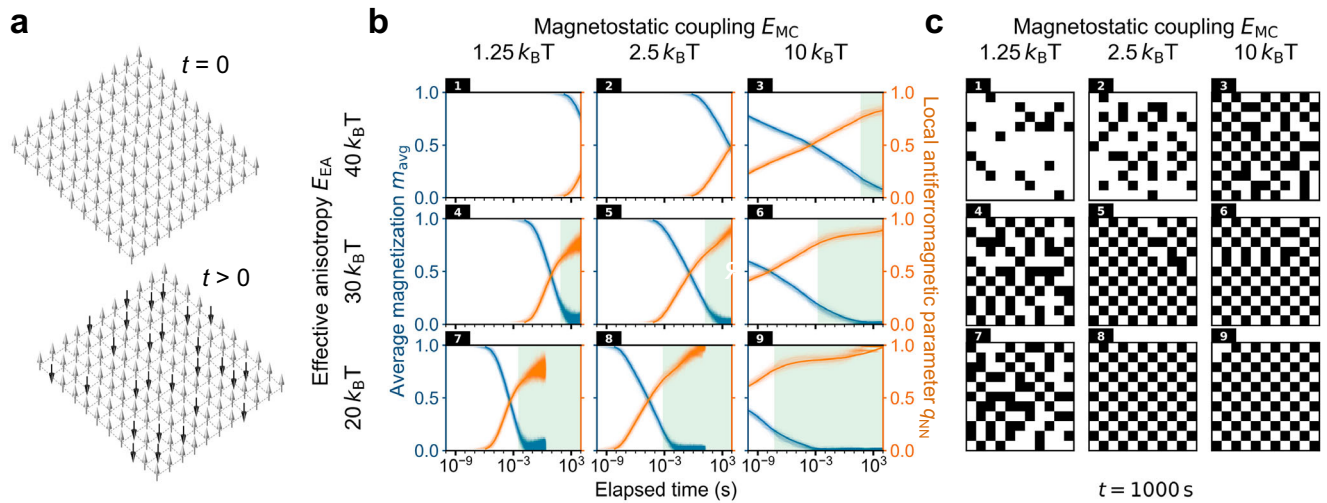
Fig. 1 | Dependence of the ordering timescale on the energy balance in a 2D Ising square lattice. a Schematic of the system with 11×11 spins. It is initialized to a uniform magnetic state with all spins pointing up and then released at $t = 0$. The lattice then relaxes to lower energies for $t > 0$. This system size was chosen because it matched the size of our fabricated systems discussed later. **b** Evolution of the local antiferromagnetic parameter q_{NN} and the average magnetization m_{avg} for different effective anisotropy E_{EA} and magnetostatic coupling E_{MC}. 20 simulations (fine lines) and their average (bold line) are shown for each case. The green-shaded region highlights the second stage of ordering where the slope of q_{NN} decreases and involves the reversal of spins within the domain boundaries. The simulations are stopped after 1000 s and the resulting magnetic states are shown in **c**. **c** Magnetic states at $t = 1000$ s. Here white (black) contrast corresponds to the up (down) spins. Panels 1–9 correspond to those of **b**.

great interest for a variety of combinatorial problems[46]. In addition, energy minimization and state dynamics in 2D Ising lattices bear similarities to equivalent processes in the human brain[50], providing a basis for computational models of the brain[50,51] and several types of neural networks such as Boltzmann machines[52] or Hopfield networks[53].

Here, we create for the first time a lattice of magnets with out-of-plane anisotropy that spontaneously orders at room temperature. We focus on a 2D square lattice of Ising spins (Fig. 1a) because of its importance for fundamental science and for applications. By fabricating such lattices with nanomagnets with various diameters and separations, and made from precisely tuned multilayer films with different number and thicknesses of the layers, we have been able to determine both theoretically and experimentally how the energy landscape of the system defines its ordering dynamics. Utilizing this information, we have engineered the timescale of the system response, which provides a means to tailor the arrays for specific computing applications.

Results

Relating the energy landscape to the magnetic relaxation timescale with Monte Carlo simulations

We begin with a theoretical exploration of the degree and timescale of spontaneous ordering in a square 2D Ising system and how it is influenced by the energy landscape of the spins. For this, we performed kinetic Monte Carlo simulations using the "Hotspice" package[54]. The system simulated was a lattice of 11×11 magnetostatically (dipolarly, in this case) coupled Ising spins (Fig. 1a) in contact with a heat bath of temperature T. The lattice was first initialized in a state with all spins pointing up (upper panel of Fig. 1a) and allowed to relax for 1000 seconds. This time was chosen to match the approximate time between the initialization and measurement of the experimental system discussed later, with the average magnetization m_{avg} and local antiferromagnetic parameter q_{NN} tracked during this period. We define q_{NN} as $(1 - \langle S_i S_{i+1} \rangle)/2$, where $\langle S_i S_{i+1} \rangle$ is the nearest-neighbour correlation, and the mean switching time of a spin j at a time t is given by the Néel-Arrhenius law[55–57]:

$$\tau_j(t) = \tau_0 \exp\left(\frac{\Delta E_j(t)}{k_B T}\right) \tag{1}$$

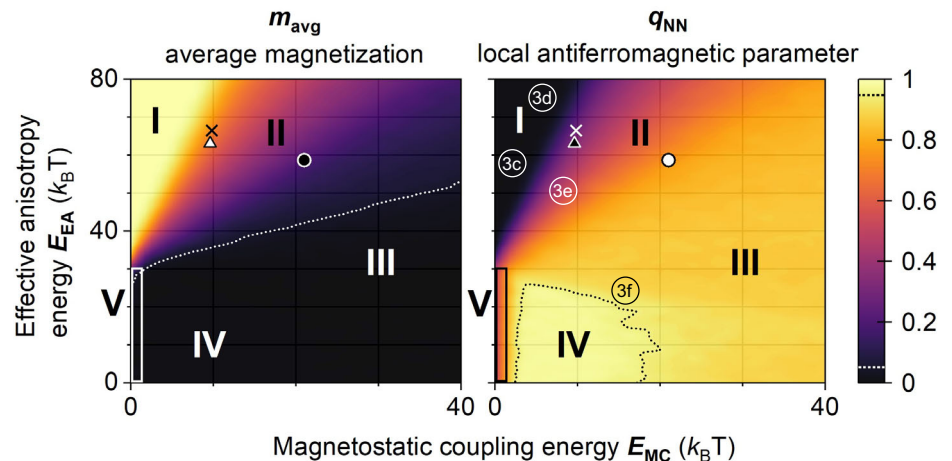Here t is elapsed time, $\tau_0 = 10^{-10}$s is the attempt period and $\Delta E_j(t)$ is the energy barrier

$$\Delta E_j(t) = E_{EA}\left(1 + \text{rand}(j)\right) + E_{MC} \sum_{i,j} S_i(t) D_{ij} S_j(t), \tag{2}$$

defined by a configuration of spins S_i at every time step, magnitude of the point dipolar interaction D_{ij} between spins i and j, a random $\pm 5\%$ Gaussian variation of anisotropy rand(j) for different spins[24,58], as well as a time-independent effective anisotropy energy E_{EA} and energy associated with the dipolar coupling between the nearest neighbour spins E_{MC} (see Supplementary Note 1 for details).

The initial switching of individual nanomagnets is promoted by dipolar interactions with other nanomagnets in the lattice given by $E_{MC} \sum_{i,j} S_i(t) D_{ij} S_j(t)$ but, as the system assumes a more ordered state, this term decreases in value. This results in an exponential increase of the switching time due to the exponential term in Eq. 1. Simulations carried out for several sets of E_{EA} and E_{MC} confirm the universally logarithmic dependence of m_{avg} and q_{NN} on the elapsed time (Fig. 1b). An increase in E_{MC} (see columns in Fig. 1b) extends the relaxation dynamics over a longer timescale, while changing E_{EA} (see rows in Fig. 1b) does not change the slope of the curves and only shifts them along the time axis. Irrespective of the E_{EA} and E_{MC}, the spin lattices achieve $m_{avg} \sim 0$ (blue traces in Fig. 1b) earlier than perfect checkerboard ordering with $q_{NN} = 1$ (orange traces in Fig. 1b). Furthermore, as the system nears $m_{avg} \sim 0$, the ordering rate decreases, which can be seen by the decrease in the slope of the orange lines as they enter the green-shaded regions in Fig. 1b. Snapshots of the magnetic state at $t = 1000$ s (Fig. 1c) provide a clue to why this two-stage ordering process occurs (reflected by the two different slopes in q_{NN}). Panels 1 and 2 in Fig. 1c are snapshots of the system during the rapid change of both m_{avg} and q_{NN} in the first phase of the ordering. Here, individual nanomagnets throughout the system switch (Panel 1) followed by domains of antiferromagnetic ordering starting to form (Panel 2). These doubly degenerate domains expand to completely fill the system (Panel 3 and 4) with boundaries forming between the domains with nanomagnets of opposite polarity (Panels 5 and 6).

From this point on, a further increase in q_{NN} can only be achieved by switching the nanomagnets in the domain boundaries. As these magnets are now stabilized through the dipolar interactions with their neighbours that

Fig. 2 | Phase diagrams of the average magnetization m_{avg} and the local antiferromagnetic parameter q_{NN} as a function of effective anisotropy E_{EA} and magnetostatic coupling E_{MC} at $t = 1000$ s. Five regions can be distinguished: I – frozen state, II – transient states, III – state with domains and domain boundaries, IV – checkerboard ordering, V – superparamagnetic state. The white (black) dotted line corresponds to $m_{avg} = 0.05$ ($q_{NN} = 0.95$). Labels 3c-3f correspond to the energy landscapes shown in Fig. 3c–f. The three symbols correspond to the experimental lattices with nanomagnet diameter $D_{NM} = 170$ nm, Co thickness $t_{Co} = 1.45$ nm and nanomagnet separation $S_{ASI} = 20$ nm (circle), $S_{ASI} = 25$ nm (triangle), $S_{ASI} = 30$ nm (cross). The experimental magnetic configurations of these systems are shown in Fig. 4.

have already switched, the energy barrier for them to switch is considerably higher than at the beginning of the relaxation process. This increases the switching time exponentially (see Eq. 1) and slows down further ordering. The details of this process are elaborated in Supplementary Note 2. A consequence of the two-stage ordering is that, while a stronger coupling E_{MC} promotes faster demagnetization $m_{avg} \rightarrow 0$ (e.g., see blue lines in Panels 7–9 of Fig. 1b, where the time to get to $m_{avg} \sim 0$ decreases from $\sim 10^{-2}$ to $\sim 10^{-3}$), it does not necessarily result in faster ordering $q_{NN} \rightarrow 1$ (orange lines in Panels 7–9 of Fig. 1b) as it increases the stabilization of the magnetic states in the domain boundaries. Therefore, E_{MC} must not exceed a certain upper limit for the system to order on a given timescale and to not dwell in a metastable state with $m_{avg} \sim 0$ and $q_{NN} < 1$.

The dependence of m_{avg} and q_{NN} on E_{EA} and E_{MC} at $t = 1000$ s is summarized in the phase diagrams of Fig. 2. In Region I, neither m_{avg} nor q_{NN} experience a notable change compared to the initial state due to the strong anisotropy and weak magnetostatic coupling (corresponding to Panel 1 in Fig. 1c). Increase of the E_{MC}/E_{EA} ratio shifts the system through the transient Region II, characterised by decreasing average magnetization and increasing ordering (corresponding to Panel 2 in Fig. 1c). Further increase of E_{MC}/E_{EA} shifts the system to Region III with $m_{avg} \sim 0$ and q_{NN} still not 1, characteristic for the second ordering stage (corresponding to Panel 6 of Fig. 1c). Any further increase of E_{MC}/E_{EA} does not affect the average magnetization or ordering at $t = 1000$ s. Achieving the high ordering of Region IV, given by the dotted black line that envelops a region with $q_{NN} \geq 0.95$ in Fig. 2 (exemplified by Panels 8 and 9 in Fig. 1c), requires lowering both E_{MC} and E_{EA} below a certain threshold. The narrow Region V (enclosed by vertical box in Fig. 2) is the regime in which the spins are superparamagnetic at the chosen timescale. The border between Regions V and I at $E_{MC} = 0$ is therefore a transition between the superparamagnetic and frozen regimes. This border is located at $E_{EA} \sim 30\ k_BT$ because nanomagnets with such an effective anisotropy have an average switching time of ~ 1000 s (the time point of these diagrams). Region IV with $q_{NN} \sim 1$ is, therefore, constrained from the left by the superparamagnetic regime, from the top by the frozen regime, and from the right by states in which switching spins in domain boundaries is too energetically expensive.

The phase diagrams in Fig. 2 are snapshots at $t = 1000$ s and, with increasing time, the boundaries between the different regions will shift. Because of this, if the observation time is long enough and E_{MC} is non-negligible, a system located in the frozen region at $t = 1000$ s may eventually find itself in the more ordered Regions II, III or IV (see phase diagrams for $t \sim 27$ months in Supplementary Note 3). The state of the nanomagnet array is therefore defined by E_{EA}, E_{MC} and t. Practical applications exploiting systems with specific dynamics defined by E_{EA} and E_{MC} require careful adjustment of the lattice and nanomagnet dimensions, as well as the stack

materials and layer thicknesses. We show how this can be achieved in the next section.

Designing the energy landscape of coupled Co/Pt nanomagnets

Artificial spin ices with perpendicular magnetic anisotropy that are thermally-active at room temperature on experimentally measurable timescales have not been realized before. The first reason for this is that achieving large E_{MC} for this geometry is harder due to the confinement of demagnetizing fields in the vicinity of the nanomagnet (central magnet in Fig. 3a) compared to the in-plane case (leftmost magnet in Fig. 3a). The second reason is that balancing the energy contributions to E_{EA}, required to lower the energy barrier to switching, is equally challenging in Co/x (x = Pt, Pd, Ni) multilayers. To address these challenges, we focused on precisely controlling E_{EA} in perpendicular nanomagnets and maximizing E_{MC} between them.

We fabricated the nanomagnets from Co/Pt ferromagnetic multilayers, which are widely used because of their strong perpendicular magnetic anisotropy[59]. The primarily interfacial origin of the anisotropy allowed us to vary E_{EA} and E_{MC} almost independently by changing the number of Co/Pt interfaces and the thickness of the Co layers, respectively. We have calculated the energy landscape of a pair of nanomagnets to guide the selection of nanomagnet diameter D_{NM}, separation S_{ASI}, number of Co layer repetitions N_{Co}, and thicknesses of Co and Pt layers, t_{Co} and t_{Pt}, respectively (Fig. 3b). We allowed the magnetization to rotate coherently in one nanomagnet ($\vec{M}_\theta$ in Fig. 3b) while keeping the other fixed ($\vec{M}_{fixed}$ in Fig. 3b). The energy was then calculated for polar angles θ from 0° to 180° and included four energy terms associated with the uniaxial interfacial anisotropy, demagnetization, magnetostatic interaction between the layers in the nanomagnet and the dipolar coupling between the nanomagnets (see Supplementary Note 4 for details). The resulting energy landscape provides an estimate of the energy barrier that the system needs to overcome to go from the higher-energy magnetic state with parallel moments to the lower-energy antiparallel state.

In Fig. 3c, we show the energy landscape for a pair of coupled nanomagnets made of (Co [0.5] / Pt [1.0])$_2$ / Co [0.5] layers with $N_{Co} = 3$, $D_{NM} = 200$ nm and $S_{ASI} = 20$ nm, where the numbers in square brackets are thicknesses in nm. Such stacks have a high anisotropy and are widely used for spintronics applications[60,61] due to the high thermal stability, which provides more than 10 years of retention time (a measure of how long a device can store information reliably without the nanomagnet switching) even in sub-20 nm diameter nanomagnets[60]. The small number of ferromagnetic Co layers, as well as their low thickness, results in a localized demagnetizing field (central magnet in Fig. 3a), minimizing crosstalk between the nanomagnets. Both properties–high anisotropy and low crosstalk–while useful for information storage applications, contradict the high-E_{MC}, low-E_{EA} requirements of a lattice to give fast spontaneous
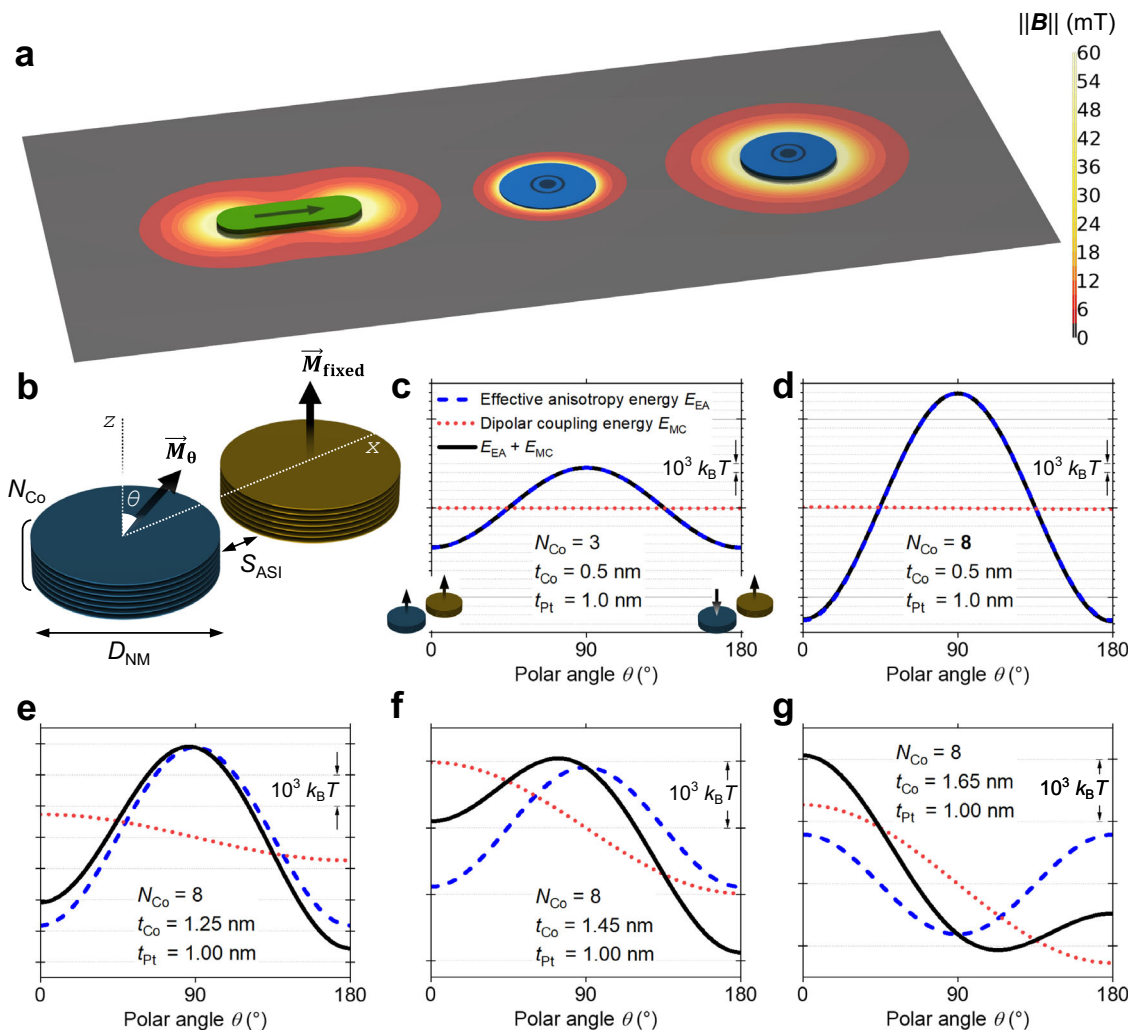
Fig. 3 | Dependence of the energy landscape of multilayered nanomagnets with perpendicular magnetic anisotropy on the material stack and lateral dimensions. **a** Magnitude of the magnetic flux density for a permalloy nanomagnet (dimensions: $100 \times 300 \times 20$ nm^3) with in-plane anisotropy (left) and 200 nm-diameter nanomagnets with perpendicular magnetic anisotropy consisting of 3 Co layers of 0.5 nm thickness (centre) and 8 Co layers of 1.45 nm thickness (right). The Co layers are separated by 0.8 nm of vacuum. **b** Schematic showing the geometrical parameters used in energy landscape calculations. **c–g** Energy landscapes calculated for the system shown in **b** for $D_{NM} = 200$ nm, $S_{ASI} = 20$ nm and different Co layer thicknesses. The vertical scale is energy, where k_B is the Boltzmann constant and $T = 300$ K.

ordering. Arrays of nanomagnets made of such a stack are located in the "frozen" Region I of Fig. 2 ("3c" label).

To devise a high-E_{MC}, low-E_{EA} stack, we varied N_{Co} and t_{Co} while fixing the nanomagnet diameter D_{NM} and separation S_{ASI}. S_{ASI} should be minimized to maximize the dipolar coupling, and was set to 20 nm, which was the smallest nanomagnet separation we were able to obtain with confidence when fabricating nanomagnet arrays with electron beam lithography. D_{NM} was set to 200 nm, which was the largest possible nanomagnet diameter that did not result in the formation of multidomain states. This upper threshold value for D_{NM} was determined experimentally by observing the magnetic states in multiple lattices of nanomagnets fabricated with different diameters.

Increasing the number of Co layer repetitions N_{Co} from 3 to 8 produces a stack similar to those used in previous works on artificial spin ices with out-of-plane nanomagnets[25–29], with the energy landscape shown in Fig. 3d. E_{MC} is approximately quadratically proportional to the total Co thickness and increases by a factor of ~7. However, the increased number of Co/Pt interfaces results in a higher anisotropy, as seen in Fig. 3c, d, and the system remains in Region I of Fig. 2 ("3d" label). Achieving an E_{MC}-dominated lattice requires the lowering of E_{EA} without decreasing E_{MC}. For this, one needs to consider the two additional components of E_{EA} beyond the interfacial anisotropy: the demagnetization energy and dipolar coupling

between layers of the stack. The dipolar coupling between the layers is rather weak and increases the perpendicular anisotropy, and thus cannot be used to lower E_{EA}. In contrast, the demagnetization energy is considerable and decreases E_{EA}. The demagnetization energy increases with Co thickness, just like E_{MC}, which has the same physical origin. Therefore, increasing t_{Co} to 1.25 nm results in a reduction in E_{EA} and an increase in E_{MC} (Fig. 3e), shifting the system towards Region II of Fig. 2 ("3e" label). At $t_{Co} = 1.45$ nm (Fig. 3f), $E_{MC} \sim E_{EA}$, which results in a highly asymmetric landscape with the lowest E_{EA} and highest E_{MC} among the considered stacks. Such an energy landscape should facilitate spontaneous ordering and, depending on the absolute values of E_{EA} and E_{MC}, an array of such nanomagnets belongs to Region III or IV of Fig. 2 ("3f" label). The demagnetizing field of these nanomagnets (rightmost nanomagnet in Fig. 3a) has a similar extent to that of the Permalloy nanomagnets typically implemented for in-plane artificial spin ices (leftmost nanomagnet in Fig. 3a). Further increase of t_{Co} to 1.65 nm results in the shift of the energy minimum to $\theta \sim 110°$, indicating a loss of perpendicular anisotropy (Fig. 3g).

From calculations, we have shown the effect on the energy landscape of changing the experimental system in terms of layer thicknesses, as well as the nanomagnet diameters and separations. By comparing this to the results from our Monte Carlo simulations, we are then able to predict how changing the system parameters will influence the relaxation timescale. This has
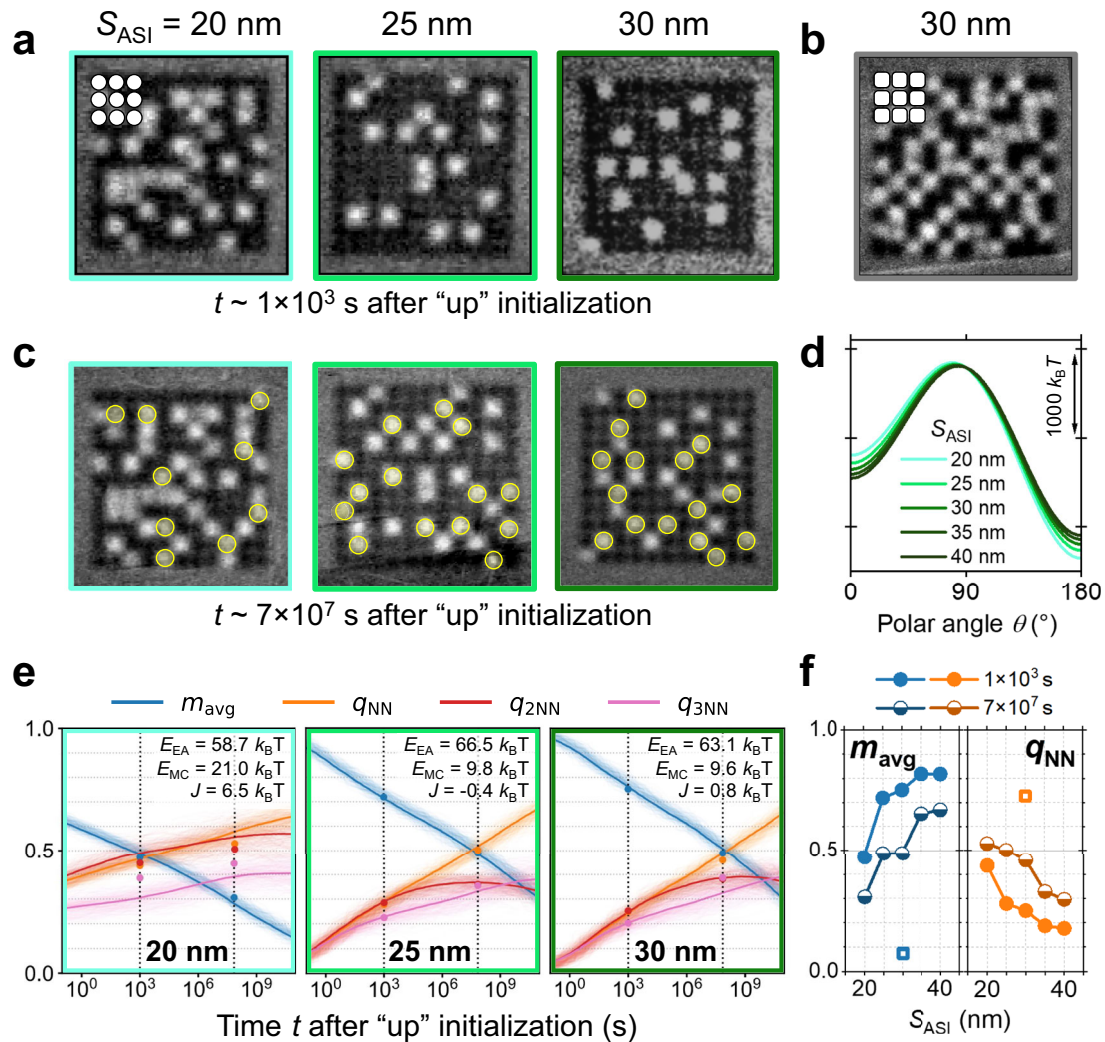
Fig. 4 | Observing the dependence of the ordering timescale on nanomagnet separation and nanomagnet shape with MFM. All systems were initialized to a uniform magnetic state with an out-of-plane magnetic field before the measurements. **a** MFM images of lattices with $t_{Co} = 1.45$ nm, $D_{NM} = 170$ nm and increasing nanomagnet separation S_{ASI} observed at $t \sim 1000$ s after initialization. Black nanomagnets are in the initial magnetic state while white nanomagnets have switched. Image frame colours match those of the corresponding curves in **d** and frames in **e**. **b** Array of 170 nm-wide square nanomagnets separated by 30 nm observed at $t \sim 1000$ s. $t_{Co} = 1.45$ nm as in **a**. The nanomagnet shape is shown in the top left inset. All other results are for circular nanomagnets as shown in the top left inset of **a**. **c** The same nanomagnet arrays as in **a** observed after ~27 months at room temperature. The magnets that have switched during this time are highlighted with yellow circles. **d** Energy landscapes calculated for the lattices shown in **a**. **e** Evolution of average magnetization m_{avg} and local antiferromagnetic parameters q_{NN}, q_{2NN}, q_{3NN}. The fine lines are calculated using Monte Carlo simulations, the bold lines are their averages, and the points are experimental data. **f** Average magnetization m_{avg} and local antiferromagnetic parameter q_{NN} as a function of S_{ASI} determined from the MFM images. Data for **a**–**c** are represented as filled circles, open squares and semi-filled circles, respectively. MFM images for $S_{ASI} = 35$ and 40 nm can be found in Supplementary Note 5.

enabled us to experimentally realize square lattices of interacting out-of-plane nanomagnets with the ability to control the ordering timescales from sub-seconds to years, as we show in the following section.

Control of relaxation timescales in experimental dipolar-coupled 2D Ising systems

We now turn to experimental systems where limitations in fabrication impose additional constraints on the system design. For example, achieving small S_{ASI}—a key parameter influencing E_{MC}—becomes more challenging as the thickness of the stack increases, so we limit N_{Co} to 7. Another effect is that the Pt spacer layers may become discontinuous on decreasing their thickness below ~0.4 nm and, to be sure that we have a continuous layer we choose $t_{Pt} = 0.8$ nm for the experimental systems, unless otherwise mentioned. These parameters permitted an S_{ASI} down to 20 nm, and we varied S_{ASI}, D_{NM} and t_{Co} in the experiment.

The multilayers of Ta[3] / Pt[4] / (Co[t_{Co}] / Pt[0.8])₆ / Co[t_{Co}] / Ru[2] were deposited by magnetron sputtering on Si substrates with a natural

oxide layer. They were patterned into square lattices of 11×11 nanomagnets by electron beam lithography and Ar ion milling. For transport measurements, the Ta/Pt bottom layer was patterned into Hall bars. Magnetic force microscopy (MFM) was used to measure the magnetic state after applying an out-of-plane magnetic field of 0.9 T to initialize all nanomagnets to an "up state". For the MFM measurements, we covered the samples with a 60 nm-thick Poly(methyl methacrylate) resist to minimize the influence of the stray magnetic field of the MFM probe on the sample.

We first looked at arrays of nanomagnets with $t_{Co} = 1.45$ nm, $D_{NM} = 170$ nm and different S_{ASI}. The state of the arrays at time $t \sim 1000$ s after initialization is shown in Fig. 4a. Black contrast indicates that the nanomagnets are in the state initialized by magnetic field, while white contrast indicates nanomagnets that have spontaneously switched. The number of switched nanomagnets gradually decreases with increase in S_{ASI}. Since S_{ASI} has no effect on E_{EA} and only changes E_{MC}, this result is easy to interpret. The decrease of E_{MC} at a constant E_{EA} lowers the asymmetry of the energy landscape by making the initial energy well deeper and therefore
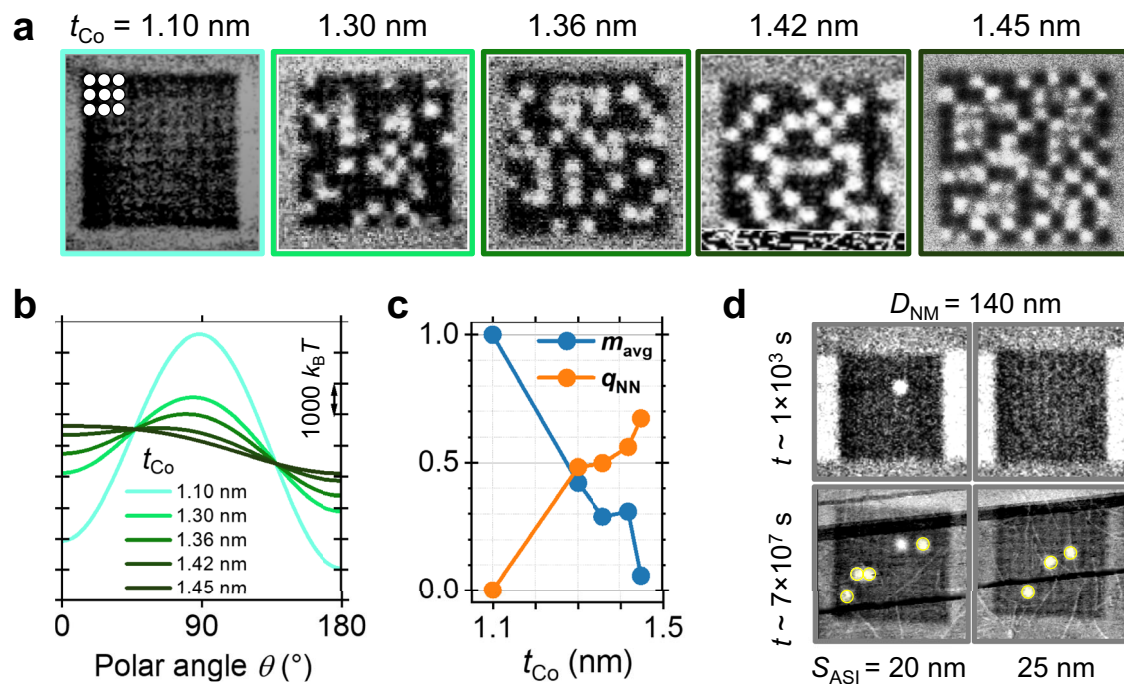
Fig. 5 | Dependence of ordering on the Co layer thickness and the nanomagnet size observed with MFM. All systems were initialized to a uniform magnetic state (black contrast) with an out-of-plane magnetic field before the measurements. **a** MFM images of lattices with D_{NM} = 200 nm, S_{ASI} = 20 nm and increasing Co thickness t_{Co} observed at $t \sim 1000$ s. Image frame colours correspond to those of the curves in **b**. White contrast indicates that the nanomagnets have switched. **b** Energy landscapes calculated for the lattices shown in **a**. **c** Average magnetization m_{avg} and local antiferromagnetic parameter q_{NN} as a function of t_{Co} determined from MFM images in **a**. **d** MFM images of lattices with D_{NM} = 140 nm and t_{Co} = 1.45 nm observed at $t \sim 1000$ s and $t \sim 7 \times 10^7$ s. The nanomagnets that have switched between the two times are indicated with yellow circles.

harder to leave ($\theta = 0°$ in Fig. 4d) while making the lower-energy well shallower ($\theta = 180°$ in Fig. 4d).
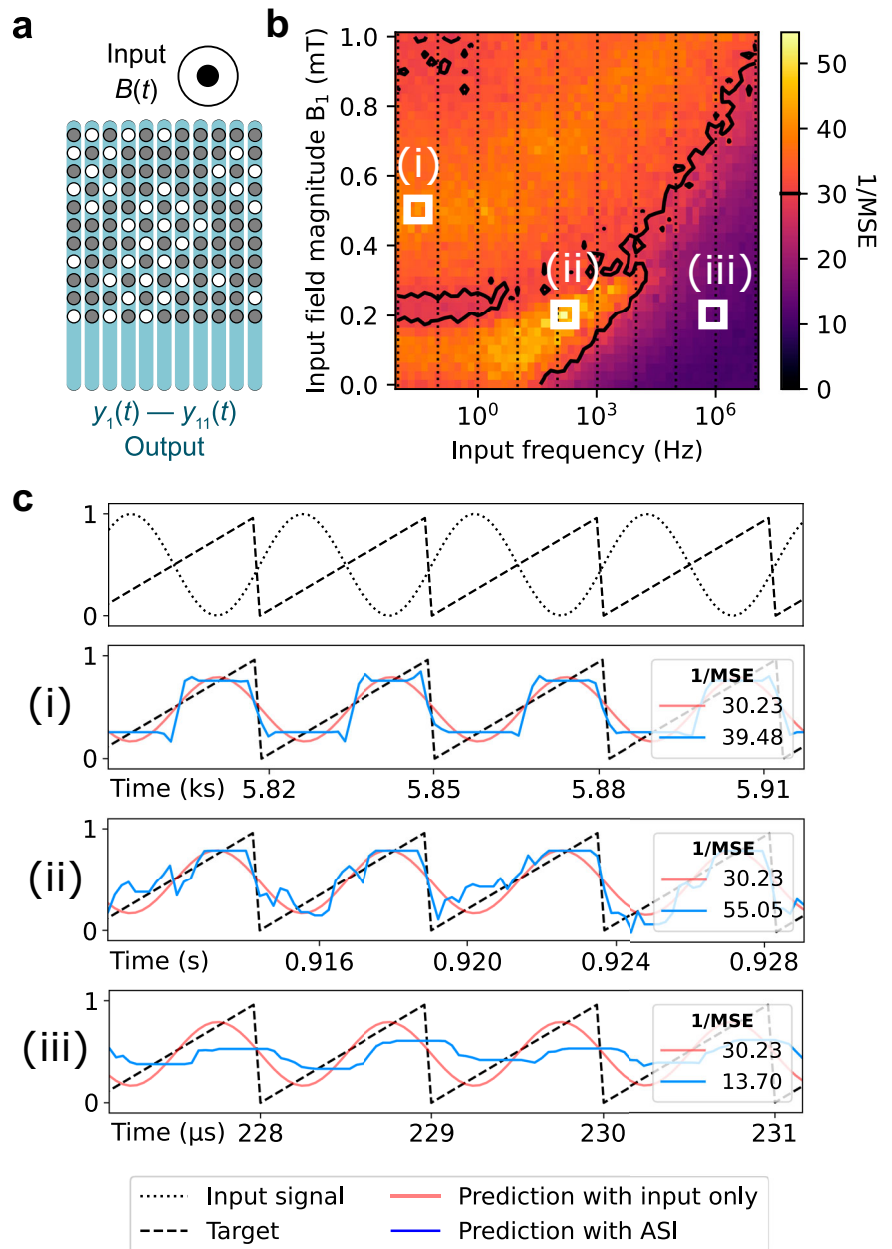
From the MFM images, we calculated the average magnetization m_{avg} and local antiferromagnetic parameter q_{NN} as defined above. With decreasing S_{ASI}, the monotonic increase in q_{NN} and decrease in m_{avg} (filled circles in Fig. 4f; MFM images for 35 and 40 nm are shown in Supplementary Note 5) highlight the important role that the magnetostatic coupling plays in the spontaneous ordering. We do not reach $q_{NN} = 1$, $m_{avg} = 0$, characteristic of highly ordered states since a further decrease of S_{ASI} is challenging in terms of the fabrication. Instead, we changed the shape of the nanomagnets from circular to square with rounded corners (compare insets in Fig. 4a, b) without modifying the stack. The resulting closer proximity of the magnets produces higher E_{MC} and a substantial increase in ordering (MFM image in Fig. 4b; m_{avg} and q_{NN} shown as a square data point in Fig. 4f).

The m_{avg} and q_{NN} of a 2D Ising system with any E_{EA} and E_{MC} will evolve with time (see, for example, Fig. 1b). Therefore, one can achieve a higher degree of ordering simply by waiting long enough. To confirm this, we kept the nanomagnet arrays at room temperature in ambient atmosphere and no magnetic field for ~27 months, which is equivalent to ~7×10^7 s. We then remeasured the samples without applying any magnetic field and observed the states shown in Fig. 4c (additional intermediate magnetic states are shown in Supplementary Note 5). The nanomagnets that have additionally switched are highlighted by yellow circles. There was no switching of nanomagnets from white to black (i.e. back to the state initialized 27 months prior). The new m_{avg} and q_{NN} are shown in Fig. 4f with half-filled circles. The decrease in m_{avg} and increase in q_{NN} indicate the additional ordering of the lattice, and one can make use of the evolution of these parameters to pinpoint location of the lattices on the phase diagrams of Fig. 2. For this, we calculated m_{avg}, q_{NN} as well as local antiferromagnetic parameters q_{2NN} and q_{3NN} for the 2nd and 3rd nearest neighbours from the MFM images for $t = 1000$ s and $t = 7 \times 10^7$ s. We then fitted these values with

$m_{avg}(t)$, $q_{NN}(t)$, $q_{2NN}(t)$ and $q_{3NN}(t)$ calculated using Monte Carlo simulations with the "Hotspice" package[54], and using E_{EA}, E_{MC} and the ferromagnetic exchange coupling between the magnets J as variables (see Supplementary Note 5 for details). The fitted results are shown in Fig. 4e. The non-zero J in the case of S_{ASI} = 20 nm ($J \sim 6.5$ mT) may indicate incomplete separation of the nanomagnets in the bottom Co layer. The near-zero J for S_{ASI} = 25 and 30 nm suggests that the magnets are fully separated. The location of the fitted results on the phase diagrams of Fig. 2 (circles, triangles and crosses for S_{ASI} = 20, 25 and 30 nm, respectively) indicates that the achieved levels of E_{MC} are sufficient for a complete ordering (Region V) in $t \sim 1000$ s but E_{EA} is too high. Note that these phase diagrams were calculated assuming that there is no exchange coupling between the nanomagnets, so $J = 0$. Therefore, since the S_{ASI} = 20 nm "circle" experimental point is for the lattice with $J \sim 6.5$ mT, its location is approximate.

Having looked at the effect of S_{ASI} and time t on ordering in the system, we then looked at the influence of t_{Co} and D_{NM}. MFM images taken at $t \sim 1000$ s of the nanomagnet arrays with D_{NM} = 200 nm, S_{ASI} = 20 nm and varying t_{Co} from 1.1 nm to 1.45 nm are shown in Fig. 5a. As we have seen, t_{Co} has a profound effect on E_{EA} and E_{MC} (Fig. 3e–g), and consequently on the ordering timescale. Indeed, as t_{Co} increases, the corresponding energy landscapes become more asymmetric (Fig. 5b) and, from the MFM images, we find that m_{avg} decreases while q_{NN} increases (Fig. 5c). Increasing D_{NM} to 200 nm provides a lower m_{avg} and higher q_{NN} (0.06 and 0.67, respectively; see data for t_{Co} = 1.45 nm in Fig. 5c) than for the same lattice with D_{NM} = 170 nm (0.47 and 0.44, respectively; see data for S_{ASI} = 20 nm in Fig. 4f). However, further increase of D_{NM} to 230 nm in the same stack results in formation of multidomain states within the nanomagnets, providing an upper limit to D_{NM}. Conversely, a decrease of D_{NM} to 140 nm slows down the ordering process so that there is hardly any switching at $t \sim 1000$ s (top images in Fig. 5d) and only a few reversed magnets at $t \sim 7 \times 10^7$ s (bottom images in Fig. 5d). We have therefore experimentally confirmed that D_{NM}

Fig. 6 | Monte Carlo simulations of the performance of an 11 × 11 lattice reservoir for a sine to sawtooth signal transformation. The parameters used for the simulations are $E_{MC} = 2.5\ k_BT$, $E_{EA} = 20$ $k_BT \pm 5\%$ and $B_0 = -0.35$ mT. **a** Schematic of the lattice used as a reservoir. Blue readout lines indicate the row-by-row averaged magnetic state readout. **b** Inverse mean squared error 1/MSE as a function of the input magnetic field frequency and amplitude B_1. Higher (lower) values in yellow (purple) indicate better (worse) performance. The black contours correspond to 1/MSE ~ 30, highlighting regions where the reservoir performs better than the linear transformation of the original input signal. **c** Temporal view of the transformation. The upper panel shows the input sinewave signal (black dotted curve) and the target sawtooth signal (black dashed line). Shown in the lower three panels are the prediction with and without the artificial spin ice (ASI) reservoir (blue and red curve, respectively) for different input frequencies with the target sawtooth signal given for comparison (black dashed line).

and t_{Co} have a profound effect on the ordering dynamics of the lattice with t_{Co} requiring a precise adjustment to achieve a low enough E_{EA} (as shown in Fig. 3d-g). The out-of-plane anisotropy of the nanomagnets means that the state of the nanomagnets can be directly accessed with electrical readout using the anomalous Hall effect. To demonstrate this, we performed electrical measurements on lattices with $D_{NM} = 140$ and 170 nm and $S_{ASI} = 30$ and 40 nm on timescales of tens of seconds, which showed similar degrees of thermal activity to the lattices measured with MFM (Supplementary Note 6).

We have now demonstrated experimentally that the relaxation dynamics of out-of-plane spin lattices can be engineered with careful tuning of the anisotropy of and magnetostatic coupling between the nanomagnets by altering their dimensions, separation and shape, as well as the stack layer thicknesses. We have provided numerical evidence that the timescale associated with the collective dynamics can be tuned all the way from sub-seconds to years. This opens up unexplored avenues for optimising the performance of reservoir computing systems incorporating these lattices as we show in the next section.

Tuneable-frequency reservoir computing with 2D Ising systems

The 2D Ising system is an appealing platform for a variety of computational approaches. Short-term memory and reset of the system after processing an input play a central role in brain-inspired computing[62,63], and both of these properties can be achieved by exploiting the dynamics of m_{avg} and q_{NN} that we presented above. This ability to tune the dynamics is particularly important in reservoir and probabilistic computing where, in contrast to conventional von Neumann computing, higher frequencies are not inherently beneficial. Instead, the priority lies in matching the dynamics of the physical system to the timescale of incoming data patterns since this is the only way that the physics of the system can be effectively harnessed for data processing. To demonstrate the effect of frequency matching on the computational performance, we have simulated a signal transformation task using our 2D Ising system for reservoir computing.

Reservoir computing is a framework for neural networks that makes use of a system with non-linear behaviour called a "reservoir" to map input data into a higher-dimensional space, in which the inputs can be separated by a

linear transformation. The reservoir does not need to be trained (so it is not modified itself) but does need to be a system with short-term memory and high dimensionality[62,64], properties that are met by many physical systems[20,21,24,64–69]. Here we employ Monte Carlo simulations using the "Hotspice" package[54] to simulate the performance of a reservoir comprising the 2D Ising system on transforming sine waves of different frequencies into a sawtooth signal, a task that is often used to test the nonlinearity of a reservoir[69,70].

For the reservoir, we employed the 11×11 lattice with $E_{EA} = 20$ $k_BT \pm 5\%$ and $E_{MC} = 2.5 k_BT$ (Panel 8 of Fig. 1b). We have experimentally demonstrated electrical readout of m_{avg} in the 11×11 lattices using the anomalous Hall effect (see Supplementary Note 6), and therefore we implemented this magnetic state readout method in the simulations. The input for the simulations was applied in the form of an out-of-plane magnetic field $B(t)$ acting on the entire system (Fig. 6a) and was scaled such that its magnitude extends from B_0 (minimum) to B_1 (maximum) as shown in the top panel of Fig. 6c. Accordingly, the energy barrier term of Eq. 2 was extended to include the Zeeman term associated with the applied magnetic field as follows:

$$\Delta E_j(t) = E_{EA}\big(1 + \text{rand}(j)\big) + E_{MC} \sum_{i,j} S_i(t) D_{ij} S_j(t) + E_{Zeeman}\big(B(t), j\big) \quad (3)$$

The average magnetization of each lattice column was used for the readout $y_i(t)$ (Fig. 6a). A discussion about the experimental feasibility of such a grid of local readouts is given in Supplementary Note 7. The readout was used to perform a linear regression $o(t) = \sum_{i=1}^{n} w_i y_i(t)$ and transformation[71,72], where i is the nanomagnet array column number, w_i is the associated weight, $o(t)$ is the predicted signal and $n = 11$ is the array dimension. The inverse mean squared error (1/MSE) between $o(t)$ and the desired result (the sawtooth) was used as a performance metric.

The 1/MSE for a range of frequencies and amplitudes of the input magnetic fields B_1 is shown in Fig. 6b. The black contour indicates a threshold of 1/MSE ~ 30, which can be achieved using only a linear transformation without a reservoir. The best results (ii) are achieved at the input frequency of ~100 Hz. For other frequencies (e.g. at (i) 0.05 Hz and (iii) 100 kHz), the performance is noticeably worse and cannot be improved to the same level by altering the input field magnitude B_1 (Fig. 6b). Interestingly, the best performance is achieved at frequencies around the transition between the first ($m_{avg} > 0$) and the second ($m_{avg} \sim 0$, $q_{NN} \rightarrow 1$) ordering stages of the lattice (Panel 8 of Fig. 1b). A low-frequency input corresponds to the longer relaxation time (green-shaded region of Panel 8 in Fig. 1b) and allows the system to reach the same state with $m_{avg} \sim 0$ regardless of the input data. This results in a square rather than a sawtooth signal after the transformation (blue trace in panel (i) of Fig. 6c). For a high-frequency input (panel (iii) in Fig. 6c), the lattice cannot respond fast enough to the changes in the signal and cannot reproduce the rise or the sudden drop of the sawtooth. At an optimal input frequency (ii), the system achieves an MSE comparable to other magnetic reservoirs[69]. The performance can be further improved by increasing the size of the lattice or introducing a gradient in the effective anisotropy (see Supplementary Note 8).

In summary, we have demonstrated that the performance of the 2D Ising reservoir depends on how well the ordering dynamics matches the frequency of the input. This is characteristic for this type of computation and, therefore, the ease with which one can engineer the relaxation timescale in the 2D Ising lattices is highly advantageous. This avoids the otherwise necessary and computationally expensive preprocessing of the input data[65,68,70,73].

Discussion

We have shown with Monte Carlo simulations that the timescale of the relaxation dynamics in 2D Ising lattices can be tuned by varying the effective anisotropy and magnetostatic coupling, and that this can be exploited to achieve an enhanced performance of these lattices for reservoir computing.

This information allowed us to fabricate experimental arrays of magnetostatically-coupled perpendicular nanomagnets with the desired properties by engineering the energy landscape through careful selection of materials and geometries.

We have shown that we can achieve a high degree of spontaneous ordering in arrays of out-of-plane nanomagnets. Nevertheless, achieving such a high level of ordering on an even shorter timescale as well as reaching $q_{NN} = 1$ would be beneficial. Placing our experimental results on the ordering phase diagrams in Fig. 2 reveals a way to do so. Indeed, Region IV with $q_{NN} \sim 1$ is located below the experimental points (circle, triangle and cross in Fig. 2) indicating sufficient E_{MC} and excessive E_{EA}. Therefore, in order to achieve a perfect ordering at a given timescale, we need a method to tune E_{EA} with more precision. While we have shown that E_{EA} can be reduced by increasing the magnetic layer thickness t_{Co}, going beyond the nominal sub-0.1 nm precision of t_{Co} used in this work is challenging. Therefore, to control the perpendicular magnetic anisotropy in Co/Pt multilayers more precisely in the future, one can use thermal annealing[74–77]. Furthermore, laser annealing[78,79] would provide a means to locally modify E_{EA} and create spatially complex designs.

In addition to making permanent modifications to the magnetic properties, E_{EA} can be temporarily changed by applying current. The generated spin-orbit torque does not lift the degeneracy of "up" and "down" magnetic states in the out-of-plane easy axis geometry[80,81]. Therefore, on application of a current, the Joule heating and spin-orbit torque (requiring the lattice to be placed on an appropriate layer) lower the energy barrier to switching without interfering with the E_{MC}-driven ordering. Experimental confirmation of this is detailed in Supplementary Note 9. Using voltage and current to reduce E_{EA} would provide a way to dynamically change the relaxation timescale of the lattice, opening the way to create systems with an adaptive temporal response, which is a cornerstone of information processing in the brain[82,83] and brain-like computing[84,85]. In addition, by engineering the current density distribution (as discussed in Supplementary Note 7) or by applying a voltage to individual nanomagnets[86], a more local electrical control could be achieved.

We have shown that, by careful choice of the layer number and thicknesses in out-of-plane artificial spin lattice, a magnetostatic coupling energy E_{MC} of tens of k_BT can be obtained. The ability to create systems with such high coupling provides an alternative, more energy efficient method to link the nanomagnets compared with the external electronic connections often used in probabilistic computing schemes[49,87] or for time multiplexing in reservoir computing[65,68]. For such applications, a further increase in E_{MC} could be beneficial and can be accomplished by adding a soft magnetic layer with in-plane anisotropy underneath the out-of-plane lattice[28]. We tested this approach on square arrays of nanomagnets with $D_{NM} = 140$ nm and observed a substantial increase in the spontaneous ordering (Supplementary Note 10). Another approach to increase E_{MC} is to optimise the shape of the nanomagnets (Supplementary Note 11). Such control of the coupling by altering the shape is uniquely suited to out-of-plane nanomagnets since, for in-plane magnets, a change of shape tends to give a change in the distribution of the demagnetization field.

This freedom to control both E_{EA} and E_{MC} locally will provide a means to create lattices with novel emergent properties. In terms of fundamental science, this means that the thermodynamics can now be studied with different lattice geometries to reveal new phases and phase transitions. In addition to creating thermally-active out-of-plane systems, it will now be possible to pattern mixed lattices incorporating both thermally-active in-plane and out-of-plane nanomagnets. These do not necessarily have an equivalent in bulk crystal systems and are likely to display unusual collective phenomena.

In terms of applications, these time-dependent artificial spin lattices of perpendicular nanomagnets offer an exciting platform for reservoir or probabilistic computing in square or other more complex geometries. The fact that these systems can be electrically interfaced, adapted to the input frequency and have short-term memory based on thermal

activity, means that they have all the properties required for next generation computing.

Our work therefore opens vistas across the fields of spintronics, reservoir computing and artificial spin ice, providing precise control of the cooperative behaviour and a flexibility in the design that can be finely tuned for different computing applications.

Methods

Sample fabrication
The films were deposited at room temperature onto high-resistivity Si wafers with a natural oxidation layer using DC magnetron sputtering. A base pressure of $\leq 1 \times 10^{-8}$ Torr and Ar gas pressure of 3 mTorr were used for the sputtering. The deposited films were processed into devices with electron beam lithography and Ar ion milling. 50 nm-thick 2% hydrogen silsesquioxane was used as an electron beam resist to achieve high-resolution patterning of the nanomagnets. A milling current of 60 mA and angle of 5° were used. Poly(methyl methacrylate) 4% 950k was used as an electron beam resist for patterning the Hall bars and electrodes.

MFM measurements
All MFM measurements were performed at room temperature. Low-moment Bruker MESP-V2-LM probes were used. The samples were initialized by applying three 5-second-long pulses of a 0.9 T out-of-plane magnetic field, sufficient to saturate them and give a uniformly magnetized state on removing the magnetic field before the MFM measurements were carried out. Care was taken to make sure that there was no lateral magnetic field component or remanent magnetization associated with the magnetic field source that would affect the state of the nanomagnet arrays. All MFM scans were performed at zero field.

Energy landscape calculations
The energy landscapes were calculated in Mathematica using a custom code. The profiles were calculated for the polar angle of magnetic moment of the nanomagnet going from 0° to 180° in 1° steps. To obtain the saturation magnetization of 1063 kA/m and interfacial anisotropy of 1.46 mJ m^{-2} used for the energy landscape calculations, the thin films were measured using superconducting quantum interference device vibrating sample magnetometry (SQUID VSM). Details of the energy landscape calculations are given in Supplementary Note 4.

"Hotspice" Monte Carlo simulations
The relaxation of the 2D Ising lattices and reservoir capability were simulated in Python using a custom "Hotspice" Monte Carlo code and employing a magnetic moment of 2.37×10^{-16} A m^2 for each spin and a temperature of 300 K. 600 input periods were used for the linear regression. 400 input periods were used to test the performance of the signal transformation. Details of the simulations are given in Supplementary Note 1.

Data availability

Code availability

References
1. Heyderman, L. J. & Stamps, R. L. Artificial ferroic systems: novel functionality from structure, interactions and dynamics. *J. Phys.: Condens. Matter* **25**, 363201 (2013).
2. Nisoli, C., Moessner, R. & Schiffer, P. Colloquium: Artificial spin ice: designing and imaging magnetic frustration. *Rev. Mod. Phys.* **85**, 1473–1490 (2013).
3. Skjærvø, S. H., Marrows, C. H., Stamps, R. L. & Heyderman, L. J. Advances in artificial spin ice. *Nat. Rev. Phys.* **2**, 13–28 (2019).
4. Perrin, Y., Canals, B. & Rougemaille, N. Extensive degeneracy, Coulomb phase and magnetic monopoles in artificial square ice. *Nature* **540**, 410–413 (2016).
5. Mengotti, E. et al. Real-space observation of emergent magnetic monopoles and associated Dirac strings in artificial kagome spin ice. *Nat. Phys.* **7**, 68–74 (2011).
6. Ladak, S., Read, D. E., Perkins, G. K., Cohen, L. F. & Branford, W. R. Direct observation of magnetic monopole defects in an artificial spin-ice system. *Nat. Phys.* **6**, 359–363 (2010).
7. Morrison, M. J., Nelson, T. R. & Nisoli, C. Unhappy vertices in artificial spin ice: New degeneracies from vertex frustration. *New J. Phys.* **15**, 045009 (2013).
8. Wang, R. F. et al. Artificial 'spin ice' in a geometrically frustrated lattice of nanoscale ferromagnetic islands. *Nature* **439**, 303–306 (2006).
9. Gilbert, I. et al. Emergent ice rule and magnetic charge screening from vertex frustration in artificial spin ice. *Nat. Phys.* **10**, 670–675 (2014).
10. Gliga, S. et al. Emergent dynamic chirality in a thermally driven artificial spin ratchet. *Nat. Mater.* **16**, 1106–1111 (2017).
11. Hofhuis, K. et al. Real-space imaging of phase transitions in bridged artificial kagome spin ice. *Nat. Phys.* **18**, 699–705 (2022).
12. Sendetskyi, O. et al. Continuous magnetic phase transition in artificial square ice. *Phys. Rev. B* **99**, 214430 (2019).
13. Anghinolfi, L. et al. Thermodynamic phase transitions in a frustrated magnetic metamaterial. *Nat. Commun.* **6**, 8278 (2015).
14. Cowburn, R. P. & Welland, M. E. Room temperature magnetic quantum cellular automata. *Science* **287**, 1466–1468 (2000).
15. Arava, H. et al. Computational logic with square rings of nanomagnets. *Nanotechnology* **29**, 265205 (2018).
16. Imre, A. et al. Majority logic gate for magnetic quantum-dot cellular automata. *Science* **311**, 205–208 (2006).
17. Arava, H. et al. Engineering relaxation pathways in building blocks of artificial spin ice for computation. *Phys. Rev. Appl.* **11**, 054086 (2019).
18. Gypens, P., Leliaert, J. & Van Waeyenberge, B. Balanced Magnetic Logic Gates in a Kagome Spin Ice. *Phys. Rev. Appl.* **9**, 034004 (2018).
19. Caravelli, F. & Nisoli, C. Logical gates embedding in artificial spin ice. *New J. Phys.* **22**, 103052 (2020).
20. Nomura, H. et al. Reservoir computing with dipole-coupled nanomagnets. *Jpn. J. Appl. Phys.* **58**, 070901 (2019).
21. Edwards, A. J. et al. Passive frustrated nanomagnet reservoir computing. *Commun. Phys.* **6**, 215 (2023).
22. Penty, A. & Tufte, G. A representation of artificial spin ice for evolutionary search. in *Proc. Conference on Artificial Life* (MIT Press, 2021).
23. Jensen, J. H., Folven, E. & Tufte, G. Computation in artificial spin ice. in *Proc. Conference on Artificial Life* 15–22 (MIT Press, 2018).
24. Jensen, J. H. & Tufte, G. Reservoir computing in artificial spin ice. in *Proc. Conference on Artificial Life* 376–383 (MIT Press, 2020).
25. Kempinger, S. et al. Imaging the stochastic microstructure and dynamic development of correlations in perpendicular artificial spin ice. *Phys. Rev. Res.* **2**, 012001 (2020).
26. Zhang, S. et al. Perpendicular magnetization and generic realization of the Ising model in artificial spin ice. *Phys. Rev. Lett.* **109**, 087201 (2012).
27. Fraleigh, R. D. et al. Characterization of switching field distributions in Ising-like magnetic arrays. *Phys. Rev. B* **95**, 144416 (2017).
28. Kempinger, S. et al. Field-Tunable Interactions and Frustration in Underlayer-Mediated Artificial Spin Ice. *Phys. Rev. Lett.* **127**, 117203 (2021).
29. Mengotti, E. et al. Dipolar energy states in clusters of perpendicular magnetic nanoislands. *J. Appl. Phys.* **105**, 113113 (2009).

30. Neumann, A. et al. Influence of long-range interactions on the switching behavior of particles in an array of ferromagnetic nanostructures. *New J. Phys.* **16**, 083012 (2014).

31. Pfau, B., Günther, C. M., Hauet, T., Eisebitt, S. & Hellwig, O. Thermally induced magnetic switching in bit-patterned media. *J. Appl. Phys*. **122**, 043907 (2017).

32. Pfau, B. et al. Origin of magnetic switching field distribution in bit patterned media based on pre-patterned substrates. *Appl. Phys. Lett*. **99**, 062502 (2011).

33. Coldea, R., Tennant, D. A., Tsvelik, A. M. & Tylczynski, Z. Experimental Realization of a 2D Fractional Quantum Spin Liquid. *Phys. Rev. Lett.* **86**, 1335–1338 (2001).

34. Chisnell, R. et al. Topological magnon bands in a kagome lattice ferromagnet. *Phys. Rev. Lett.* **115**, 147201 (2015).

35. Taniguchi, S. et al. Spin gap behavior of S = 1/2 Quasi-two-dimensional system CaV_4O_9. *J. Phys. Soc. Japan* **64**, 2758–2761 (1995).

36. Wannier, G. H. Antiferromagnetism. The triangular Ising net. *Phys. Rev.* **79**, 357 (1950).

37. Smerald, A., Korshunov, S. & Mila, F. Topological aspects of symmetry breaking in triangular-lattice Ising antiferromagnets. *Phys. Rev. Lett.* **116**, 197201 (2016).

38. Onsager, L. Crystal statistics. I. A two-dimensional model with an order-disorder transition. *Phys. Rev.* **65**, 117–149 (1944).

39. Cipra, B. A. An Introduction to the Ising Model. *Am. Math. Mon.* **94**, 937–959 (1987).

40. De las Cuevas, G. & Cubitt, T. S. Simple universal models capture all classical spin physics. *Science* **351**, 1180–1183 (2016).

41. Karimipour, V. & Zarei, M. H. Algorithmic proof for the completeness of the two-dimensional Ising model. *Phys. Rev. A* **86**, 052303 (2012).

42. Van den Nest, M., Dür, W. & Briegel, H. J. Completeness of the classical 2D Ising model and universal quantum computation. *Phys. Rev. Lett.* **100**, 110501 (2008).

43. Gu, M. & Perales, Á Encoding universal computation in the ground states of Ising lattices. *Phys. Rev. E* **86**, 011116 (2012).

44. Kohler, T. & Cubitt, T. Translationally Invariant Universal Classical Hamiltonians. *J. Stat. Phys.* **176**, 228–261 (2019).

45. Torquato, S. Toward an Ising model of cancer and beyond. *Phys. Biol.* **8**, 015017 (2011).

46. Lucas, A. Ising formulations of many NP problems. *Front. Phys.* **2**, 1–14 (2014).

47. Gupta, S., Ray, A. & Phoha, S. Generalized Ising model for dynamic adaptation in autonomous systems. *EPL* **87**, 10009 (2009).

48. Mohseni, N., McMahon, P. L. & Byrnes, T. Ising machines as hardware solvers of combinatorial optimization problems. *Nat. Rev. Phys.* **4**, 363–379 (2022).

49. Si, J. et al. Energy-efficient superparamagnetic Ising machine and its application to traveling salesman problems. *Nat. Commun.* **15**, 3457 (2024).

50. Ruffini, G. & Deco, G. The 2D Ising model, criticality and AIT. Preprint at https://doi.org/10.1101/2021.10.21.465265 (2021).

51. Ezaki, T., Watanabe, T., Ohzeki, M. & Masuda, N. Energy landscape analysis of neuroimaging data. Energy landscape analysis of neuroimaging data. *Phil. Trans. R. Soc. A.* **375**, 20160287 (2017).

52. Klein, M. W., Enrich, C., Wegener, M. & Linden, S. Second-Harmonic Generation from Magnetic Metamaterials. *Science* **313**, 502–504 (2006).

53. Hopfield, J. J. Neural networks and physical systems with emergent collective computational abilities. *Proc. Natl. Acad. Sci. USA.* **79**, 2554–2558 (1982).

54. Maes, J. et al. The design, verification, and applications of Hotspice: a Monte Carlo simulator for artificial spin ice. *Comp. Phys. Commun.* **313**, 109643 (2025).

55. Bean, C. P. & Livingston, J. D. Superparamagnetism. *J. Appl. Phys.* **30**, S120–S129 (1959).

56. Brown, W. F. Thermal fluctuations of a single-domain particle. *Phys. Rev.* **130**, 1677–1686 (1963).

57. Néel, L. Théorie du traînage magnétique des ferromagnétiques en grains fins avec application aux terres cuites. *Ann. de Géophys.* **5**, 99–136 (1949).

58. Daunheimer, S. A., Petrova, O., Tchernyshyov, O. & Cumings, J. Reducing disorder in artificial kagome ice. *Phys. Rev. Lett.* **107**, 167201 (2011).

59. Carcia, P. F. Perpendicular magnetic anisotropy in Pd/Co and Pt/Co thin-film layered structures. *J. Appl. Phys.* **63**, 5066–5073 (1988).

60. Ishikawa, S. et al. Co/Pt multilayer-based magnetic tunnel junctions with a CoFeB/Ta insertion layer. *J. Appl. Phys.* **115**, 17C719 (2014).

61. Jinnai, B. et al. Spin-orbit torque induced magnetization switching in Co/Pt multilayers. *Appl. Phys. Lett.* **111**, 102402 (2017).

62. Kurenkov, A., Fukami, S. & Ohno, H. Neuromorphic computing with antiferromagnetic spintronics. *J. Appl. Phys.* **128**, 010902 (2020).

63. Kurenkov, A. et al. Artificial neuron and synapse realized in an antiferromagnet/ferromagnet heterostructure using dynamics of spin–orbit torque switching. *Adv. Mater.* **31**, 1900636 (2019).

64. Tanaka, G. et al. Recent advances in physical reservoir computing: a review. *Neural Netw* **115**, 100–123 (2019).

65. Torrejon, J. et al. Neuromorphic computing with nanoscale spintronic oscillators. *Nature* **547**, 428–431 (2017).

66. Romera, M. et al. Vowel recognition with four coupled spin-torque nano-oscillators. *Nature* **563**, 230–234 (2018).

67. Midya, R. et al. Reservoir computing using diffusive memristors. *Adv. Intell. Syst.* **1**, 1900084 (2019).

68. Moon, J. et al. Temporal data classification and forecasting using a memristor-based reservoir computing system. *Nat. Electron.* **2**, 480–487 (2019).

69. Gartside, J. C. et al. Reconfigurable training and reservoir computing in an artificial spin-vortex ice via spin-wave fingerprinting. *Nat. Nanotechnol.* **17**, 460–469 (2022).

70. Lee, O. et al. Task-adaptive physical reservoir computing. *Nat. Mater.* **23**, 79–87 (2024).

71. Lukoševičius, M. & Jaeger, H. Reservoir computing approaches to recurrent neural network training. *Comput. Sci. Rev.* **3**, 127–149 (2009).

72. Moran, A., Frasser, C. F., Roca, M., & Rossello, J. L. Energy-efficient pattern recognition hardware with elementary cellular automata. *IEEE Transactions on Computers* **69**, 392–401 (2019).

73. Appeltant, L. et al. Information processing using a single dynamical node as complex system. *Nat. Commun.* **2**, 468 (2011).

74. Nistor, L. E., Rodmacq, B., Auffret, S. & Dieny, B. Pt/Co/oxide and oxide/Co/Pt electrodes for perpendicular magnetic tunnel junctions. *Appl. Phys. Lett.* **94**, 012512 (2009).

75. Wang, Y. et al. Effect of annealing on the magnetic tunnel junction with Co/Pt perpendicular anisotropy ferromagnetic multilayers. *J. Appl. Phys.* **107**, 09C711 (2010).

76. Honda, S., Morita, N., Nawate, M. & Kusuda, T. Annealing effects on the crystallographic and magnetic properties of Co/Pt multilayers. *J. Magn. Soc. Jpn.* **15**, 45–48 (1991).

77. Lee, T. Y., Won, Y. C., Son, D. S., Lim, S. H. & Lee, S. R. Effects of Co layer thickness and annealing temperature on the magnetic properties of inverted [Pt/Co] multilayers. *J. Appl. Phys.* **114**, 173909 (2013).

78. Riddiford, L. J., Brock, J. A., Murawska, K., Hrabec, A. & Heyderman, L. J. Grayscale control of local magnetic properties with direct-write laser annealing. Preprint at https://doi.org/10.48550/arXiv.2401.09314 (2024).

79. Wu, G. et al. Annealing effect on laser-induced magnetization dynamics in Co/Ni-based synthetic antiferromagnets with perpendicular magnetic anisotropy. *Appl. Phys. Lett.* **115**, 142402 (2019).

80. Miron, I. M. et al. Perpendicular switching of a single ferromagnetic layer induced by in-plane current injection. *Nature* **476**, 189–193 (2011).

81. Fukami, S., Anekawa, T., Zhang, C. & Ohno, H. A spin-orbit torque switching scheme with collinear magnetic easy axis and current configuration. *Nat. Nanotechnol.* **11**, 621–625 (2016).

82. Nunez, P. L., Wingeier, B. M. & Silberstein, R. B. Spatial-temporal structures of human alpha rhythms: theory, microcurrent sources, multiscale measurements, and global binding of local networks. *Hum. Brain. Mapp.* **13**, 125–164 (2001).

83. Izhikevich, E. M. & Edelman, G. M. Large-scale model of mammalian thalamocortical systems. *Proc. Natl. Acad. Sci. USA.* **105**, 3593–3598 (2008).

84. Chen, T., Wang, L., Li, J., Duan, S. & Huang, T. Improving Spiking Neural Network With Frequency Adaptation for Image Classification. *IEEE Trans. Cogn. Dev. Syst.* **16**, 864–876 (2024).

85. Abbott, L. F., DePasquale, B. & Memmesheimer, R.-M. Building functional networks of spiking model neurons. *Nat. Neurosci.* **19**, 350–355 (2016).

86. Vermeulen, B. F. et al. Electronic voltage control of magnetic anisotropy at room temperature in high-κ $SrTiO_3$/Co/Pt trilayer. *Phys. Rev. Mater.* **4**, 114415 (2020).

87. Borders, W. A. et al. Integer factorization using stochastic magnetic tunnel junctions. *Nature* **573**, 390–393 (2019).

Acknowledgements

Author contributions

A.K., L.J.H. and A.H. conceived the project. A.K. fabricated the samples, and designed and performed the experiments with support from A.H. and A.P. Analysis and interpretation of the data was done by J.M., A.K. and G.M.M. with support from all authors. J.M. and B.V.W. performed the Monte Carlo simulations and fitting of the experimental data. A.K. performed the Mathematica calculations and COMSOL simulations. A.K. and J.M. wrote the manuscript with input from all authors.

Competing interests

The authors declare no competing interests.

Additional information

Supplementary information The online version contains supplementary material available at https://doi.org/10.1038/s44172-025-00499-y.

Correspondence and requests for materials should be addressed to Aleksandr Kurenkov, Jonathan Maes or Aleš Hrabec.

Peer review information *Communications Engineering* thanks the anonymous reviewers for their contribution to the peer review of this work. A peer reviewer file is available.

Reprints and permissions information is available at http://www.nature.com/reprints

Publisher's note Springer Nature remains neutral with regard to jurisdictional claims in published maps and institutional affiliations.